Energy 221 (2021) 119833

Contents lists available at ScienceDirect

Energy

journal homepage: www.elsevier.com/locate/energy

Determination of time constants of diffusion and electrochemical processes in Polymer Electrolyte Membrane Fuel Cells

Alfredo Iranzo [a, b, *], Sergio J. Navas [c], Felipe Rosa [a, b], Mohamed R. Berber [d, e, **]

[a] Thermal Engineering Group, Energy Engineering Department, School of Engineering, University of Sevilla, Camino de Los Descubrimientos s/n, Seville, 41092, Spain
[b] Laboratory of Engineering for Energy and Environmental Sustainability, Camino de Los Descubrimientos s/n, 41092, Seville, Spain
[c] AICIA - Thermal Engineering Group, Camino de Los Descubrimientos s/n, Sevilla, 41092, Spain
[d] Chemistry Department, College of Science, Jouf University, Sakaka, 2014, Saudi Arabia
[e] Department of Chemistry, Faculty of Science, Tanta University, Tanta, 31527, Egypt

ARTICLE INFO

Article history:
Received 13 April 2020
Received in revised form
7 January 2021
Accepted 9 January 2021
Available online 13 January 2021

Keywords:
Polymer Electrolyte Membrane fuel cell
Electrochemical Impedance Spectroscopy
Time constant
Oxygen diffusion
Damköhler number
High Frequency Resistance

ABSTRACT

This work presents an experimental analysis of the time constants associated to diffusion and electrochemical processes in a 50 cm^2 Polymer Electrolyte Membrane (PEM) fuel cell. The experimental techniques and results include polarization curves and Electrochemical Impedance Spectroscopy (EIS) analysis of the fuel cell, where the time constants are determined from the analysis of the Distribution of Relaxation Times (DRT). EIS results are also used to determine the cell ohmic resistance, where High Frequency Resistance (HFR) values are calculated from the Nyquist plots. A wide range of operating conditions of the fuel cell are analysed, including back pressure (0.5 bar−1 bar), cell temperature (55 °C, 65 °C, 75 °C), reactant gases relative humidity (30%, 60%, 90%), cathode stoichiometry (λ_c 2.5−3.5), and oxygen concentration (air and pure oxygen). The effect of the operating conditions on the time constants are discussed, and Damköhler number is introduced and discussed.

1. Introduction

Fuel cells are devices where the chemical energy available in fuels is converted directly into electricity via electrochemical reactions. The high energy efficiency and the low environmental impact together with a significant technology development of fuel cells during the last few years have promoted its use as alternative clean power generation devices for portable, mobile and stationary applications [1], and its integration within energy systems [2–5] involving power generation, solar energy or geothermal energy. In particular, Polymer Electrolyte Membrane Fuel Cells (PEMFCs) present clear advantages, especially for the transportation sector [6–8], where the main developments, status, and trends and perspectives have been analysed by Alaswad et al. [9], Ahluwalia et al. [10] and Olabi et al. [11] respectively. This sector has showed a clear increase in the deployment of Fuel Cell Vehicles (FCVs) during the last few years, with extensive programmes in countries such as Japan, South Korea, China and United States or Canada [12–19]. Progress in fuel cell research and technology developments is contributing to the transition towards a new energy system where hydrogen technologies will play a significant role [20–22].

The core of PEMFCs consists of a polymer membrane and two electrodes mainly based on carbon materials [1,9,10,23]. In order to overcome the main technical barriers preventing PEMFCs from reaching its ultimate industrial goal, current research is focused on increasing both fuel cell performance and durability of the cell components and systems. Thus, there is a need to deeply understand the different mechanisms and contributions to the PEMFC performance losses and degradation processes [1,9–11,24].

Experimental diagnostics can help to understand the highly coupled and complex phenomena occurring within a fuel cell, where the polarization curve (I–V curve, plot of cell potential versus current) is the most common measurement of the performance of a fuel cell [25]. Three different regions can be observed in polarization curves of PEMFCs depending of the current density

* Corresponding author. Thermal Engineering Group, Energy Engineering Department, School of Engineering, University of Sevilla, Camino de los Descubrimientos s/n, 41092, Seville, Spain.
** Corresponding author. Chemistry Department, College of Science, Jouf University, Sakaka, 2014, Saudi Arabia.
E-mail addresses: airanzo@us.es (A. Iranzo), mrberber@ju.edu.sa (M.R. Berber).

https://doi.org/10.1016/j.energy.2021.119833

being drawn, where in each region a different phenomenon is dominating the cell potential and shape of the I–V curve: electrochemical kinetics at low current densities, ohmic resistance at medium current densities, and reactants mass transport at high current densities. However, as the polarization curve represents the integral output of the cell, the analysis of each of the phenomena indicated above is not directly observable.

On the contrary, Electrochemical Impedance Spectroscopy (EIS, also known as AC impedance spectroscopy) is a technique suitable for obtaining a breakdown of the polarization or overpotential contributions, as well as for obtaining different fuel cell parameters [25–27], understanding the limiting processes affecting the overall performance, and state-of-health determination (as in the work of Fouquet et al. [28]). As an example, when the PEMFC is subjected to an accelerated durability testing under different conditions and protocols, the potential curve changes showing different shapes based on the degradation processes occurred in both the catalyst layer and the proton conducting membrane. Wasterlain et al. [29] introduced a novel architecture of impedance spectrometer to provide efficient diagnostics of a PEMFC stack, investigating the effect of flooding/drying phenomena. Christian et al. [30] also proposed an impedance-based protocol for the fault detection and isolation of a wide set of operating conditions including low and high cathode stoichiometry or high CO concentration in the anode gas.

EIS has also been used for determining the characteristic timescales of the processes involved [31,32]. The details of the technique and the wide variety of applications of AC impedance spectroscopy for PEMFC diagnostics have been reviewed by Yuan et al. [33], Rezaei Niya and Hoorfar [34], and Ivers-Tiffée et al. [32]. During an EIS experiment, an AC signal of known amplitude and frequency is sent through the cell, and the response is analysed. The real and imaginary components of the cell impedance (Z) are obtained for all frequencies tested (typically between 0.1 Hz and 1–10 kHz). When represented in a complex diagram or Nyquist plot, parameters such as charge transfer resistance (activation polarization), mass transport resistances, or cell ohmic resistance (High Frequency Resistance, HFR) can be determined [33,34]. Typical Nyquist plots reported in the literature feature two pronounced arcs or semicircles for PEMFC impedance spectra, corresponding to charge transfer at medium frequencies (10–100 Hz) and reactant diffusion (usually in the cathode side) at low frequencies $\approx$ 1 Hz [33]. It is observed that with increasing current density the charge transfer arc progressively decreases, whereas gas diffusion becomes more dominant. The spectrum can reduce to one single arc if any of the two processes are vanished for particular operating conditions [33]. The cell resistance (i.e., the sum of all electronic resistances including bulk and contact resistances, and the proton-conduction resistance in the membrane) is determined using an AC high-frequency perturbation of typically more than 1 kHz [35]. The Z_{Re} value at $Z_{Im} = 0$ in the Nyquist plot represents the HFR value. Except the MEA conductivity which depends on temperature and mostly on humidification, all other contributions to the overall cell ohmic resistance are constant during the cell operation, and thus the variations of the measured HFR values can be attributed to variations of MEA conductivity [26,36,37].

As an alternative or complementary to the analysis of EIS spectra by means of Equivalent Circuit Modelling [32–34], the study of the distribution of relaxation times (DRT) has also proved to be a highly valuable method to determine the time constants of the different processes involved. This method was first used by Leonide et al. [38] for SOFC and later for Li-ion batteries [39]. Weiss et al. [40] applied this method for a High-Temperature PEMFC, and the recent work of Heinzmann et al. [41,42] discussed the novel application of DRT to the impedance spectra of a 1 cm^2 low temperature PEM single cell. They achieved the detailed deconvolution of the impedance spectra by using the DRT method, enabling the identification of up to five different polarization processes with their associated time constants. They proved this method to provide highly detailed information of the physical-chemical processes within the cell, which were not feasible to be determined from the impedance spectra. In addition to the thorough analysis of the works mentioned above, the present study has been based on the available DRT Tools developed by Wan et al. [43,44] for computing DRT based on Tikhonov regularization. Such DRT Tool by Wan et al. [44] was developed after investigating methods for the optimal regularization of the DRT deconvolution [45], and the effect of various discretization methods on the estimated DRT [46].

In the recent review by Tang et al. [47] focused on the progresses in the use of EIS for the in-depth analysis of PEMFCs, it is also stated that DRT is a suitable method to extract the characteristic time scales out of the EIS data measurements, as well as to deconvolute impedance spectra under different PEMFC operating conditions to separate loss processes in porous electrodes [41,42] and to separate overlapping impedance spectra.

The current work focuses on the effect of operating conditions on the time constants of the main processes occurring in PEMFCs i.e. electrochemical reaction and oxygen gas diffusion from channel to electrode across the Gas Diffusion Layer (GDL). In order to achieve these targets, the Distribution of Relaxation Times technique is applied to the experimental impedance spectra obtained for a technical cell of 50 cm^2. A comprehensive matrix of operating conditions was defined, covering the most common operating variables such as temperature, pressure, cathode stoichiometry, reactants relative humidity, and oxidant concentration. A Fuel Cell Damköhler number [31,48–51] is used to characterize the relative importance of both processes, and how this is determined by the operating conditions of the cell. This work presents the application of the DRT method for determining time constants of diffusion and electrochemical processes in PEMFCs of technical size (50 cm^2), which is a representative size between lab-scale and industry-scale fuel cells.

2. Experimental facility and methodology

2.1. Test station and fuel cell description

The experimental work was conducted with a PEM fuel cell test station designed and commissioned to the University of Sevilla by the Hydrogen and Fuel Cell Technology Testing Centre (CNH2). The test bench is devoted to the experimental testing of PEM single cells and short stacks up to 500 W, and it includes a Newton's 4th PSM1700 Frequency Response Analyzer for EIS experimental analysis. The test environment is the typical of a fuel cell test bench, with a reactant gas handling unit including humidifiers and back-pressure regulators, a cell heating/cooling unit, and an electronic load. The main elements of the test bench are presented in Appendix A. The cell voltage measurement uncertainty is ±1 mV with a sample rate of 1 Hz.

The cell consisted of graphite Bipolar Plates from ElectroChem Inc. With serpentine flow fields in both anode and cathode, arranged in a cross-flow layout with vertical cathode channels and horizontal anode channels [27]. Figure A3 in Appendix A presents the cell Bipolar Plates used for the experiments. Channel and land width is 0.71 mm and 0.86 mm respectively, and the total plate thickness is 9.5 mm.

A 50 cm^2 5-layer Membrane Electrode Assembly (MEA) was used, with 1.0 mg Pt/cm^2 in both anode and cathode electrodes (with 20 wt % Pt/C), Nafion N-212 and Gas Diffusion Layers from Toray (TP-060 without MPL) 0.19 mm thick and 78% porosity. The

through-plane resistance of the GDL is 80 mΩcm^2.

2.2. Experimental conditions

A comprehensive matrix of operating conditions was used in order to analyse the effect of the different conditions of the cell performance and EIS characteristics. All the conditions tested were referenced with respect to a benchmark case, which is defined as following: P_{cell} = 0.5 bar (rel), T_{cell} = 65 °C, Relative Humidity (RH) at anode and cathode = 60%. Stoichiometric factors at anode (λ_a) and cathode (λ_c) 1.3 and 2.5 respectively. Air was used as oxidant in the benchmark case. Such conditions are named according to the following nomenclature: P05_T65_a13RH60_c25RH60_air. The matrix of operating conditions is indicated in Table 1, named according to the nomenclature described above. The condition varied in each case with respect to the benchmark conditions is marked in bold and underlined in Table 1. A total of eight operating conditions were tested, where it can be observed that two pressure conditions were analysed (0.5 and 1.0 bar (rel)), three temperature conditions (55, 65, 75 °C), three RH conditions (30, 60, 90%), two values of the cathode stoichiometric factor (2.5, 3.5), and two oxidant concentrations (air, oxygen).

2.3. Description of the experimental testing procedure

The I–V polarization curves were obtained for the cell by following the experimental methodology defined in the well stablished FCTESTNET [52] and FCTESTQA [53] procedures for single cells. In particular, the test procedure consists of:

Step 1: Pre-conditioning of the cell.

The test starts by bringing the operating conditions (inputs) to the values specified for the conditioning of the cell (which are the reference conditions "P05_T65_a13RH60_c25RH60_air"). The stabilization of the conditions is done by increasing the current density by steps of 100 mA/cm^2 for the given fixed values of temperature and gas conditions, while keeping the cell voltage higher than 500 mV until reaching the current density identified for the conditioning (500 mA/cm^2).

Step 2: Setting the test conditions (test inputs).

The step starts by bringing the operating conditions to the values specified for the measurement (if not corresponding to the pre-conditioning step). The cell is maintained at 500 mA/cm^2 during 20 min and the corresponding cell voltage is measured and used as an initial reference IV point. The comparison of this first value with the cell voltage measured at the same current density during the measurement step (polarization curve) is then used as an additional indicator of the accuracy of the test.

Before starting the polarization curve, the cell voltage is brought to OCV (and, in parallel, the gas flow rates to their minimum values) for a fixed period allowing the stabilization of the operating conditions. The OCV is measured during 30 s.

Step 3: Measuring test outputs.

The measurement of the current-voltage curves is carried out in galvanostatic mode, starting at the open circuit voltage and using fixed current steps. The dwell time for each current density set point is set to 20 min (15 min for conditions stabilization and 5 min for data acquisition). The test is carried out until the voltage drops below 300 mV. The data acquisition frequency of the test bench is set to 1 s, so that each I–V point is averaged over 300 measurements.

Step 4: Data post-processing.

As mentioned before, each voltage value corresponding to a fixed current density is calculated as the average value of the last 5 min of the measurement (300 values). The standard deviation is also calculated. The reproducibility of the results was addressed by replicating the experiments, where two to three I–V curves were obtained for each condition (except for the curve with oxygen where only one experiment was carried out). The final I–V curves reported were calculated by averaging the curves obtained for each conditions, and error bars have been added to account for the standard deviation of the results measured.

The EIS impedance measurements were performed using AC signals between 0.2 Hz and 6.0 kHz, with over 14 measurements per decade. Two different signal amplitudes were tested (5% and 10% of the base intensity). The results with 10% amplitude were selected due to the better output signal behaviour observed at low frequencies.

2.4. Determination of the time constants for diffusion and electrochemical processes

The EIS spectra were used as input for the determination of the diffusion and electrochemical time constants. This was carried out using the available DRT Tools developed by Wan et al. [43,44] for computing DRT based on Tikhonov regularization. The Gauss discretization were used [45,46] with a Radial Basis Function for the discretization as proposed by Wan et al. [43]. A regularization parameter (λ) value of 1.0E-02 were defined. According to the literature [40–46], high values of the regularization parameter λ will reduce the sensitivity to the measurement errors of the overall procedure, resulting in the fact that several time constants corresponding to real processes within the fuel cell can be overridden (such as proton conduction in membrane or in the ionomer of the catalyst layers). On the contrary, a too small value of λ will drastically increase the effect of the data noise, and therefore, artefact time constants may arise originated by certain noise levels in the original EIS spectra, thus resulting in additional time constants that are actually not corresponding to real processes within the cell. In this work, given the fact that a technical size fuel cell was used and that the objective is to determine the time constants associated to the most central processes (overall electrochemical kinetics and overall reactant diffusion) a relatively large value of λ were defined (1.0E-02). More fundamental and unique processes will be overridden, but the method has proven to be effective in determining

Table 1
Operating conditions defined in the experimental tests.

Case	Pressure bar (rel)	Temperature (°C)	RH (%)	λ_a (−)	λ_c (−)	Oxidant
P05_T65_a13RH60_c25RH60_air	0.5	65	60	1.3	2.5	Air
P1_T65_a13RH60_c25RH60_air	**1.0**	65	60	1.3	2.5	Air
P05_**T55**_a13RH60_c25RH60_air	0.5	**55**	60	1.3	2.5	Air
P05_**T75**_a13RH60_c25RH60_air	0.5	**75**	60	1.3	2.5	Air
P05_T65_a13**RH30**_c25**RH30**_air	0.5	65	**30**	1.3	2.5	Air
P05_T65_a13**RH90**_c25**RH90**_air	0.5	65	**90**	1.3	2.5	Air
P05_T65_a13RH60_c**35**RH60_air	0.5	65	60	1.3	**3.5**	Air
P05_T65_a13RH60_c25RH60_**O2**	0.5	65	60	1.3	2.5	**O_2**

the time constants for the diffusion and electrochemical processes.

3. Results

The I–V polarization curves obtained for all operating conditions are represented in Fig. 1, where close-ups have been included for a better representation of the differences within the OCV region (Fig. 1, middle) and the ohmic region (Fig. 1, bottom). The corresponding power curves are represented in Fig. 2. For the sake of completeness, the pressure drop at the cathode side of the cell is reported in Appendix B.

The HFR values obtained from the EIS experiments at high frequencies (typically $Z_{im} = 0$ at 4–6 kHz) are represented in Fig. 3, whereas the average values together with the standard deviation of the measurements can be found in Table 2. HFR values were obtained from the Nyquist plots as the Z_{Re} value for $Z_{im} = 0$.

Nyquist plots for all the operating conditions analysed with the serpentine flow field are shown in Fig. 4 and Fig. 5 for different current densities: 0.2 A/cm^2, 0.5 A/cm^2, 1.0 A/cm^2, and 1.5 A/cm^2 (and 2.0 A/cm^2 where available, as not all polarization curves reached over 1.0 A/cm^2). Nyquist plots have been presented in two different arrangements for the sake of a better analysis and comparison of the results. In Fig. 4 Nyquist plots are presented in separate graphs, where each graph is containing the data corresponding to all operating conditions in Table 1 for a given current density. On the contrary, in Fig. 5 Nyquist plots are presented in separate graphs, where each graph is containing the data corresponding to all current densities for each operating condition.

Finally, Fig. 6 represents the time constants of the electrochemical (τ_{EC}) and diffusion (τ_{diff}) processes, obtained from the EIS spectra by the application of the DRT method according to Wan et al. [43,44]. The corresponding DRT graphs are included as Supplementary Material. The Damköhler number as defined by Eq. (3) is also represented in Fig. 6. Results are graphically depicted as a function of the operating conditions included in Table 1 and plotted vs. the current density. The discussion on the results obtained is presented in Section 4.

4. Discussion

4.1. Polarization curves

The experimental polarization curves in Fig. 1 are clearly presenting the three different regions typically found in fuel cells. The curve with pure reactants H_2/O_2 presents a superior performance, consistent with the fact that mass transport losses are significantly reduced when utilizing pure oxygen as oxidant [27,39,40]. Fig. 1 (middle) shows that also the OCV value is significantly higher when using pure oxygen, which is a result of the higher Nernst potential [54,55]. The second curve in terms of performance is the one corresponding to a higher cell operating pressure (1.0 bar with respect to the benchmark case operating at 0.5 bar). The positive effect of pressure on reducing activation and mass transport losses is well documented in the literature [54,55]. On the contrary, there are two conditions with a clear reduced performance, corresponding to conditions causing a dry-out of the cell i.e. low reactant relative humidity (RH 30%), and higher cell operating temperature (75 °C). Interestingly, these two polarization curves are intersecting themselves twice as observed in Fig. 1, indicating that the relative importance of each polarization losses are different for each curve as will be discussed in next sections. From the polarization curves, it can be determined that the ohmic losses are higher for the case with low relative humidity indicating a low membrane hydration until medium current densities. However once the cell achieves a higher current density (0.4–0.5 A/cm^2) the electrochemical water production is able to rehydrate the membrane and ohmic losses diminish causing a recovery in the shape of the polarization curve. This will be further discussed in the next sections.

Between the high performance and the low performance curves, there are four additional conditions where differences in the polarization curves are not that significant. The cases correspond to the benchmark conditions (P05_T65_a13RH60_c25RH60_air) and to the variations with a lower temperature (55 °C), higher cathode stoichiometry ($\lambda_c = 3.5$), and higher relative humidity (90%).

Such trend is also observed in the power curves presented in Fig. 3, with the cell using oxygen reaching up to 45 W at 2.25 A/cm^2, the cell in dry conditions (RH = 30%, T = 75 °C) reaching less than 20 W at 1.0 A/cm^2, and the other curves reaching around 25 W at 1.3–1.4 A/cm^2.

When analysing the overall performance trends with respect to variations in the operating conditions it can be observed that an increase in the operating temperature is lowering the cell performance, with 114 mV difference at 1.0 A/cm^2 between the curve at 55 °C (0.481 V) and the curve at 75 °C (0.367 V). Such difference is however not linear with respect to the temperature, but it presents instead a dramatic increase from 65 to 75 °C. It can also be observed in Fig. 1 that the differences described are becoming more pronounced as current density increases. On the contrary to the effect of temperature, the increase in the reactant relative humidity is having a positive effect on the cell performance, where the cell voltage is increasing 136 mV from RH 30% (0.381 V) to RH 90% (0.517 V) at 1.0 A/cm^2. As observed in Fig. 1, the cell performance is dramatically lower at low RH values (30%) indicating a clear dry-out of the membrane, in particular at low current densities where the cell water production is low and unable to sufficiently hydrate the membrane.

Increasing the cell backpressure is clearly beneficial for the cell performance (56 mV increase in the cell voltage from 0.5 to 1.0 bar at 1.0 A/cm^2). The benefits of operating at higher cell pressures can be observed for all range of current density (Fig. 1). In comparison, the performance increase for larger cathode stoichiometric factors is minimal, with only 18 mV increase in the cell voltage at 1.0 A/cm^2 when switching from 2.5 to 3.5 stoichiometry. However, the increase in performance is becoming larger for higher current densities, as more gas flow is providing a higher water removal capability, and a higher and more uniform oxygen concentration along the flow channels.

Clearly, the operation with pure oxygen is providing the highest cell voltage increase (138 mV at 1.0 A/cm^2), where the cell voltage improvement is becoming more pronounced as current density increases.

4.2. HFR and MEA ohmic resistance

The effect of both current density and operating conditions on the HFR value is presented in Fig. 3. The operating condition is causing a higher impact on the HFR than the current density (for the range of operating conditions tested). Consequently with the observations indicated in the previous section, there are two exceptions to this statement, that are the cases corresponding to the operation in drier conditions (RH = 30%, and T = 75 °C). Not only the HFR values are significantly higher than in the other cases, indicating a drier membrane, but also the variations with current density are more significant. At 0.2 A/cm^2 and 1.0 A/cm^2 both conditions are presenting similar HFR values, where polarization curves at such current densities were also similar (Fig. 1). However, at 0.5 A/cm^2 the HFR values are significantly different, with the highest value corresponding to the operation at low RH (30%). This is the reason why the differences in the polarization curves for both operating conditions at 0.5 A/cm^2 were so evident, whereas at

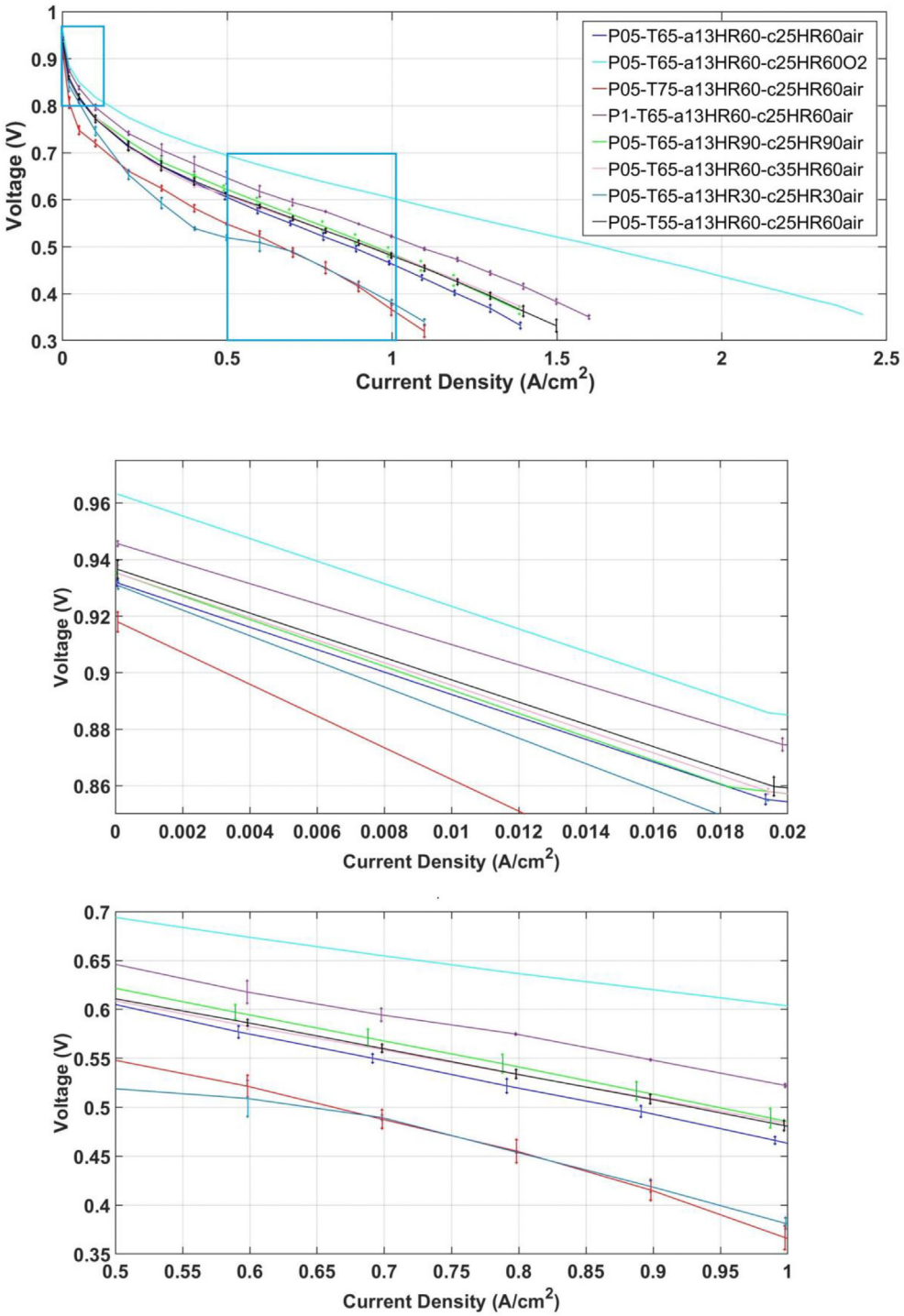

Fig. 1. Polarization curves obtained for the experimental conditions defined in Table 1. (top). Close-up in the OCV region (middle) and ohmic region (bottom). Error bars accounting for the standard deviation of the measurements are included.

lower and higher current densities both curves were again resembling to each other.

The other operating conditions are presenting much lower values of HFR (an average of 30% lower HFR), indicating a much better membrane hydration. Besides, the HFR variations with respect to current density are also less pronounced. The benchmark case and the operation with higher cathode stoichiometry result in HFR values of around 2.6 mOhm, whereas all the other operating conditions result in better membrane hydration values, with HFR values of around 2.4 mOhm.

The HFR results compare well with results reported in the literature. The effect of different parameters on HFR has been addressed by several authors such as Asghari et al. [56] or Chang et al. [57] (torque or compression ratio), Danzer and Hofer [58], Yan et al. [59], Yin and Chang [60], or Schneider et al. [61] (RH values), and Fouquet et al. [28] or Kadyk et al. [62] (dry, normal, or flooded conditions), and Yan et al. [459] (temperature effects). A summary can be found in the review work by Rezai Niya et al. [63]. The

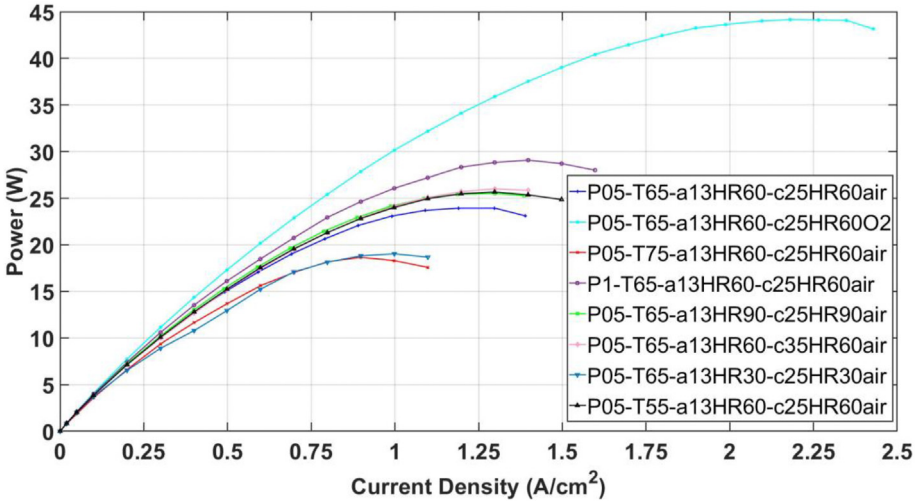

Fig. 2. Power curves obtained for the experimental conditions defined in Table 1.

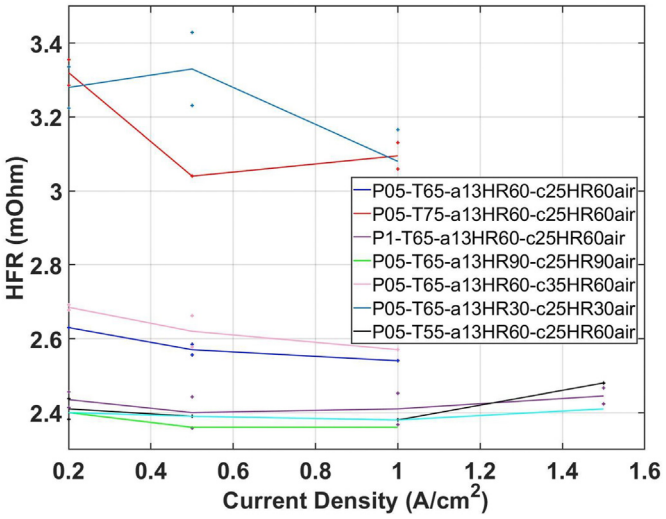

Fig. 3. High Frequency Resistance (HFR) values obtained for the operating conditions defined in Table 1, at 10 A (0.2 A/cm^2), 25 A (0.5 A/cm^2), 50 A (1.0 A/cm^2), 75 A (1.5 A/cm^2). Error bars accounting for the standard deviation of the measurements are included.

decrease in HFR observed in the experimental results when increasing the RH inlet gases conditions (Table 2) is consistent with the observations by Danzer and Hofer [58] and Yan et al. [59], and is obviously related to the improved membrane hydration when humidified gases are used. This can be particularly relevant within the anode side of the membrane, as electro-osmotic drag is transporting water towards the cathode, and back-diffusion may not be able to push water back towards the anode side, particularly for thicker membranes [64]. It is interesting to note in Fig. 3 and Table 2 that a higher operating pressure also contributes to a reduced HFR value, so that the effect of pressure is not only observable in the activation and mass transport region [54,55] but also in the ohmic region. This is due to the different amount of liquid water (with ability to hydrate the membrane) present within the cell depending on the pressure level, where it was previously shown that the cathode pressure is presenting a major effect than anode pressure [65].

It must be considered that the HFR values provided in Table 2 are the results of two contributions; first, the electric resistivity of the cell components which is constant for any operating condition as long as materials and bolts torque are kept constant, and secondly, the proton-conduction (ionic) resistance in the membrane, which is mainly depending on the membrane water content (λ) as well as on temperature although up to a lesser extent (Springer et al. [66]).

Table 2
High Frequency Resistance (HFR) values obtained for the operating conditions defined in Table 1, at 10 A (0.2 A/cm^2), 25 A (0.5 A/cm^2), 50 A (1.0 A/cm^2), 75 A (1.5 A/cm^2), 100 A (2.0 A/cm^2). Standard deviation of the measurements is indicated between parentheses. The Open Circuit Voltage (OCV) values obtained are also presented.

	HFR (mOhm) @0.2 A/cm^2	HFR (mOhm) @0.5 A/cm^2	HFR (mOhm) @1.0 A/cm^2	HFR (mOhm) @1.5 A/cm^2	HFR (mOhm) @2.0 A/cm^2	OCV (V)
P05_T65_a13RH60_c25RH60_air	2.63 (0)	2.57 (0.014)	2.54 (0)	–	–	0.932
P1_T65_a13RH60_c25RH60_air	2.435 (0.021)	2.4 (0.042)	2.41 (0.042)	2.445 (0.021)	–	0.946
P05_T65_a13RH60_c35RH60_air	2.685 (0.007)	2.62 (0.042)	2.57 (0)	–	–	0.935
P05_T55_a13RH60_c25RH60_air	2.41 (0.028)	2.39 (0)	2.38 (0)	2.48 (0)	–	0.937
P05_T75_a13RH60_c25RH60_air	3.32 (0.034)	3.04 (0)	3.095 (0.035)	–	–	0.918
P05_T65_a13RH30_c25RH30_air	3.28 (0.057)	3.33 (0.099)	3.08 (0.085)	–	–	0.931
P05_T65_a13RH90_c25RH90_air	2.4	2.36	2.36	–	–	0.935
P05_T65_a13RH60_c25RH60_O2	2.4	2.39	2.38	2.41	2.47	0.963

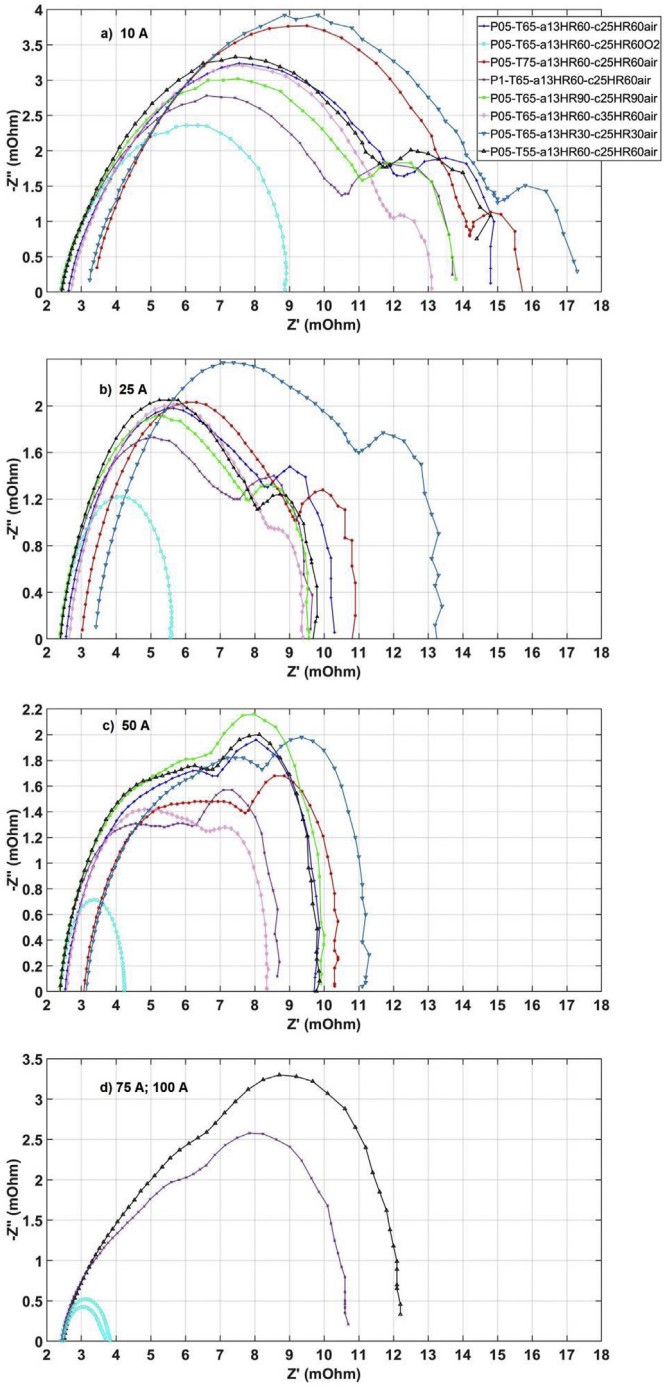

14

Fig. 4. Nyquist plots obtained for the operating conditions defined in Table 1: a) 10 A (0.2 A/cm^2), b) 25 A (0.5 A/cm^2), c) 50 A (1.0 A/cm^2), d) 75 A (1.5 A/cm^2) and 100 A (2.0 A/cm^2).

4.3. Nyquist plots

It is well known that water management is one of the key issues when it comes to ensure an improved cell performance and durability [64,67]. However, when experiencing poor cell voltages, it is not always straight-forward to determine whether a cell is dried-out or flooded. In the work by Fouquet et al. [28] it is stated that from the polarization curve alone, it is rather difficult to determine whether there are drying-out or flooding issues in case the cell voltage drops. However, the analysis of the Nyquist plots obtained from EIS results can clearly indicate both membrane drying-out or flooding (state-of-health) [33,34]. Basically, a dried-out membrane can be determined by a shift of the HFR towards higher Z_{Re} values, whereas flooding can be determined by an increase in the size of the low frequency arc.

Nyquist plots for the serpentine flow field are shown in Figs. 4 and 5. Fig. 4 presents Nyquist plots for all conditions listed in Table 1, where a unique plot is presented for each current density. Thus the effect of the different operating conditions can be better identified. On the contrary, Fig. 5 presents a Nyquist plot for each of the conditions listed in Table 1, where each plot contains the data for all current densities. Thus the effect of the current density can be better identified for each operating condition.

The first observation is that Nyquist plots are featuring the well-known two arcs representing the activation polarization (arc on the left at medium frequencies) and the concentration polarization (arc on the right at lower frequencies) [27,31,32,54,55]. At high current densities (1.0 A/cm^2, Fig. 4, bottom, and Fig. 5) both arcs are mostly overlapped, indicating that the timescales of both processes are approaching each other [32]. It is interesting to note that the operation with pure oxygen does not produce the arc or semicircle associated to concentration polarization, as mass transport losses are negligible at least up to the current density tested (2.0 A/cm^2). Indeed, it has been reported that the low frequency arc is typically missing in cells operating with pure oxygen [68]. It is also observed in Fig. 4 that there are two main starting locations in the Z_{Re} axis for the first arc, which is related to the two main ranges of HFR values identified and discussed in section 4.2, being the drier conditions the ones with low RH (30%) and high cell temperature (75 °C) as discussed previously. In general, the medium frequency arc is larger than the high frequency arc, indicating that activation polarization losses are dominating over mass transport losses. This is particularly evident at low current densities where the cathode activation losses are dominating the cell voltage loss. However, it is clearly observed in Figs. 4 and 5 that increasing the current density is lowering the size of the activation arc and increasing the size of the mass transport arc. The cathode overpotential decreases with increasing current density as there is more energy available for the electrochemical reaction to occur. Higher current densities increase the driving force for the ORR, as reported with similar experiments by Cooper and Smith [69], also showing that the medium frequency arc decreases with increasing current density.

The increase of the mass transport arc is particularly evident for current densities of 1.0 A/cm^2 and above, except for the operation with pure oxygen where no mass transport polarization is observed as discussed previously (Fig. 5, g). In addition, the activation polarization arc when operating with pure oxygen is also significantly smaller in comparison with all the other conditions operating with air (Figs. 4 and 5), as the higher oxygen concentration is increasing the exchange transfer current i_0 in the Butler-Volmer equation [27]. Among the cases operating with air, it is also interesting to note that the activation polarization arc for the operation at higher pressure (1.0 bar vs. 0.5 bar) is presenting the smallest size (lower activation polarization as a result of the beneficial effect of pressure in the Butler-Volmer equation [55].

Fig. 4 is also showing the effect of the reactant gases RH on the impedance response of the cell. At all current densities the activation polarization (represented by the medium frequency arc) is increasing for lower RH values. This is indicating that relative humidity is having an influence on the electrode kinetics, which is was previously reported by Liu et al. [70], Neyerlin et al. [71], or Xu et al. [72] based on their experimental results. This is also observed in Fig. 4 for the cases analysed. The differences are particularly

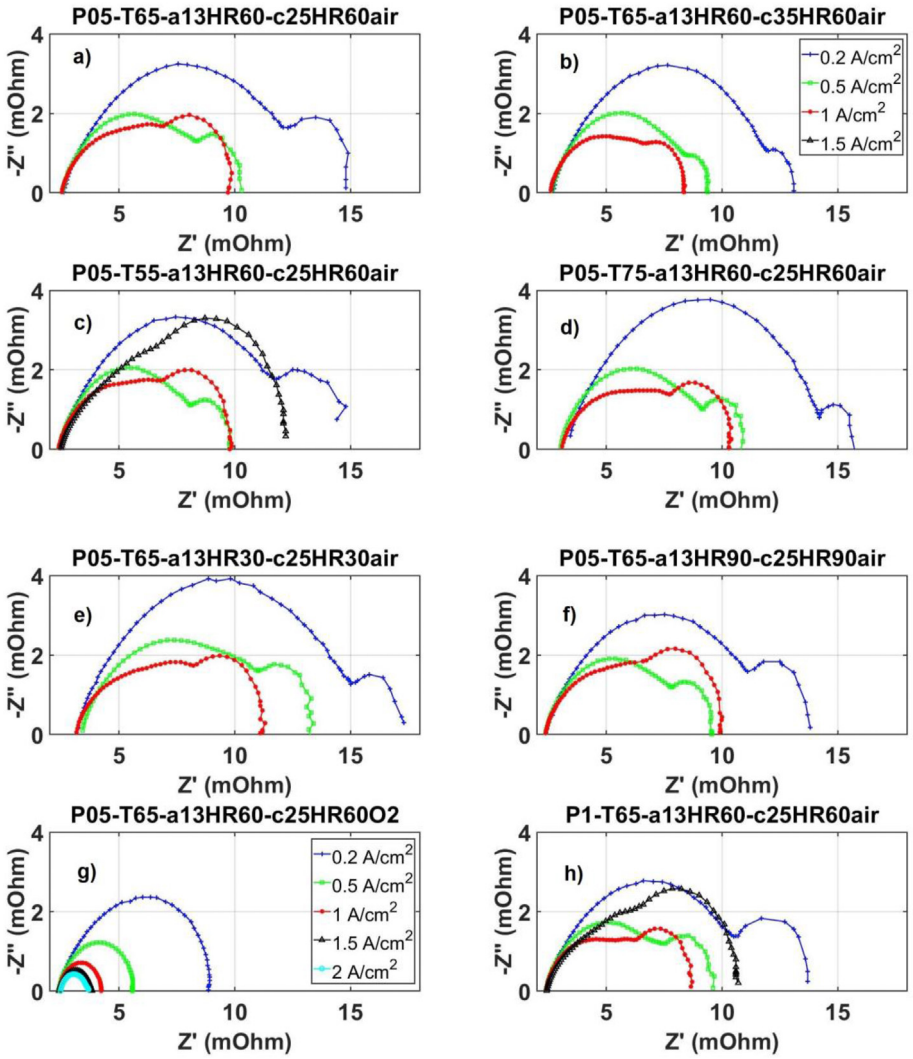

Fig. 5. Nyquist plots obtained for the operating conditions defined in Table 1: a) benchmark case, b) $\lambda_c = 3.5$, c) T = 55 °C, d) T = 75 °C, e) RH = 30%, f) RH = 90%, g) Pure Oxygen, h) 1 bar (rel).

significant at low RH (30%) rather than at high RH (90%), and the difference in the arc size is decreasing when increasing the current density, so that at 1.0 A/cm^2 the medium frequency arcs are almost the same in size, thus indicating that the effect of RH on kinetics is less pronounced at higher current densities.

4.4. Time constants of diffusion and electrochemical processes

In Fig. 6 the time constants have been depicted both for electrochemical processes (τ_{EC}, top) and diffusion processes (τ_{diff}, middle). The time constants were obtained from the Distribution of Relaxation Times (DRT, where the graphs are included as Supplementary Material). The electrochemical time constants are in the range of 0.5–5.5 ms, while the diffusion time constants are in the range of 0.05–0.25 s (threefold higher). The amount of data collected allows for a detailed analysis of how different operating conditions parameters are influencing the time constants of the electrochemical and diffusion time constants. In particular, the cell operating conditions (cell temperature and pressure, reactants RH and stoichiometry, and O_2 concentration) as well as the current density have been analysed.

The benchmark case conditions were as following: $P_{cell} = 0.5$ bar (rel), T_{cell} = 65 °C, Relative Humidity (RH) at anode and cathode = 60%. Stoichiometric factors at anode (λ_a) and cathode (λ_c) 1.3 and 2.5 respectively. Air was used as oxidant in the benchmark case. Such conditions were named according to the following nomenclature: P05_T65_a13RH60_c25RH60_air (see legend in Fig. 6).

Regarding the electrochemical time constants (τ_{EC}, Fig. 6 top) a mixed behaviour and trends can be observed. Results show that the operation with pure oxygen leads to smaller time constants, as it corresponds to the positive influence of a higher oxygen concentration on the kinetics of the electrochemical ORR reaction. Under most operating conditions the time constant associated to the electrochemical reaction is being reduced as current density increases. This is in accordance with the size reduction of the corresponding arc in the Nyquist plots (Fig. 5) and indicates that kinetic losses are decreased, which is in accordance to the Butler-Volmer equation. There are two exceptions, which are exactly corresponding to the dry conditions discussed in the previous sections (i.e. operation at higher temperature 75 °C and at low RH 30%). Under such conditions the time constant is increasing with current density. This is the result of the effects of temperature and RH on ORR kinetics. It is known that the kinetic reaction order of the ORR

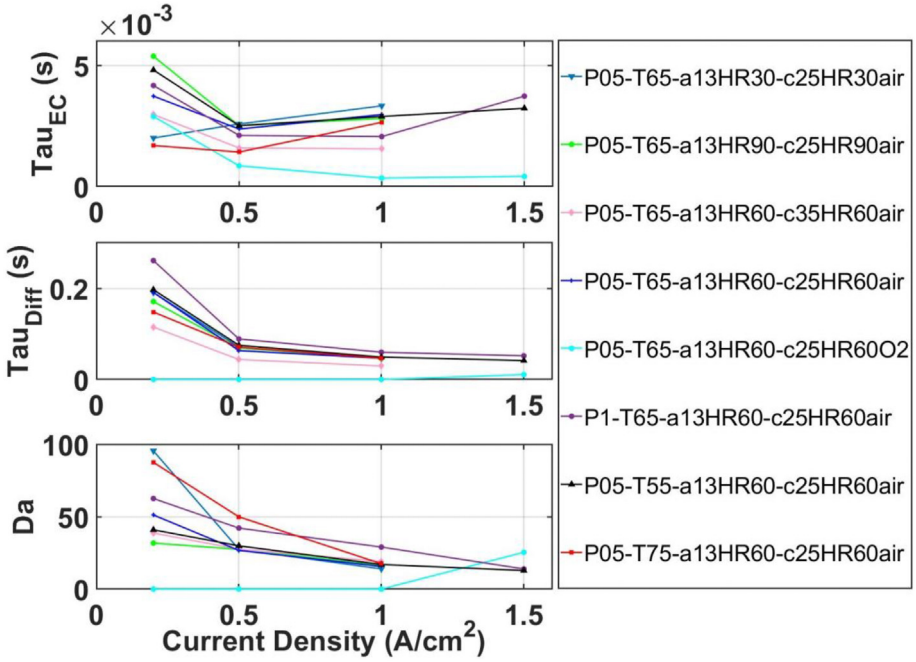

Fig. 6. Time constants obtained for the operating conditions defined in Table 1: Electrochemical time constant (top); diffusion time constant (middle). Damköhler number (bottom).

is varying with RH, where reported values of activation energy are 49 kJ/mol at 100% RH and 55 kJ/mol at 50% RH (Xu et al. [72]). Thus, lower RH values are hindering electrochemical kinetics in the ORR, and this is why dry conditions produces an increase in the electrochemical time constants. Xu et al. [72] reported that the catalytic activity is increasing with an increase in RH, in particular in the range 0–60%. The progressive increase of τ_{EC} for dry conditions as current density increases is a consequence of the further intensification of the dry-out of the cell at higher current densities, which occurs for this cell given its heat transfer issues (this is addressed in detail during the next discussion on τ_{diff}). On the other hand, a higher temperature is also enhancing electrochemical kinetics, and this is the reason why low cell temperature (55 °C) is presenting higher time constants in Fig. 6 (5 ms at 0.2 A/cm^2), followed by medium cell temperature (65 °C, with 3.8 ms), and finally a higher cell temperature (75 °C) is featuring the lowest ORR time constant (1.8 ms at 0.2 A/cm^2).

Regarding the oxygen diffusion time constants (τ_{diff}, Fig. 6 middle) several observations are noteworthy. For a deeper understanding and discussion of the results it is convenient to recover the concept of effective diffusion coefficient D_{eff} (i.e. the diffusion coefficient within the porous media of the cell considering the porous matrix of the GDL and considering the degree of water saturation) [73–76].

For determining D_{eff}, the bulk diffusion coefficient is corrected with the GDL porosity and the degree of flooding affecting the pores blockage by liquid water. The correlation from Nam and Kaviany [77] is used in the present analysis. Temperature and pressure conditions are also affecting the diffusion and must therefore also accounted as stated by Um et al. [78]. Considering all the effects influencing the effective diffusivity of reactants through the GDL, D_{eff} can be calculated as:

$$D_{eff} = D_0 \left(\frac{\varepsilon - 0.11}{1 - 0.11}\right)^{0.785} (1-s)^2 \left(\frac{P_0}{P}\right) \left(\frac{T}{T_0}\right)^{1.5} \quad (1)$$

where D_{eff} is the effective diffusion coefficient, D_0 is the bulk diffusion coefficient (at T_0, P_0), and ε is the GDL porosity. T_0 and P_0 are reference temperature and pressure, and s is the water saturation (volume fraction of liquid water). As the diffusion characteristic time τ_{diff} can be estimated as δ^2_{GDL}/D_{eff} [79] (where δ_{GDL} is the thickness of the GDL), it is concluded that a higher D_{eff} values will result in smaller time constants for the diffusion process.

When analysing the results obtained in Fig. 6 related to τ_{diff}, it can be first determined that there is no time constant associated to oxygen diffusion for the operation with pure oxygen, indicating that issues associated to mass transport processes are completely neglected (a minor value is obtained for higher current densities from 1.5 A/cm^2). This was also observed in the corresponding Nyquist plot in Fig. 5. g. Among the conditions operating with air, the smallest diffusion time constant is observed for higher cathode stoichiometry (which allows for a higher oxygen transport from channel to electrode), whereas the largest diffusion time constant is observed for operation at higher pressures. This is a consequence of the inverse proportionality of the diffusion coefficient with respect to pressure as indicated in Eq. (1). The effective diffusion coefficient is thus decreasing as the pressure increases (Um et al. [74], Eq. (1)).

It is interesting to observe that the diffusion time constant is decreasing with respect to the current density. This is at first sight contradictory as higher current densities involve more water generation, and therefore a higher water saturation in the GDL and electrodes (thus higher diffusion time constants could be expected according to Eq. (1)). The trend observed in Fig. 6 is however the opposite, while the reason for this is twofold: first, the relatively large size of the cell (50 cm^2, while still externally air-cooled) is provoking heat transfer issues as current increases. The cell temperature is measured at the external side of the bipolar plate, but the internal cell temperature is significantly higher in order to reject all heat generated to the external ambient, by conduction from the inner components of the cell, and then convection towards the ambient. This means that MEA and GDLs temperature is increasing as the current increases, and this is leading to a higher fraction of water being in gas phase as current increases. Thus, the liquid water saturation within the cell is actually diminishing

despite the fact that more water is being generated, which was experimentally determined for the same cell by means of Neutron Radiography [80]. With a less amount of liquid water, Eq. (1) results in a higher effective diffusion coefficient, and thus the related time constant τ_{diff} decreases. In addition, the higher temperature is also aiding the reduction of τ_{diff} as it also contributes to a higher effective diffusion coefficient (Eq. (1)). In order to enforce higher water saturations in the cell and try to revert this situation, the case with high RH values (90%) was further examined. Fig. 6 (middle) shows that this is actually the only case where τ_{diff} is slightly increasing after 1.0 A/cm^2.

Once the time constants of the different processes are determined a non-dimensional analysis can be derived. In particular, a Fuel Cell Damkhöler number [31,49–51] can be used so that:

$$Da_{PEMFC} = Electrochemical\ reaction\ rate / Mass\ Transfer\ rate \quad (2)$$

Which can be written as:

$$Da_{PEMFC} = \tau_{diff} \Big/ \tau_{EC} \quad (3)$$

The electrochemical reaction rate is corresponding to the Oxygen Reduction Reaction (ORR) rate, as this is generally the limiting reaction in most cases [26,55,81]. It must be however considered that this may not be correct for ultra-low Platinum loading in the anode catalyst, but kinetics is controlled by the ORR in the cell used, with 1 mgr$_{Pt}$/cm^2 in both anode and cathode electrodes. Regarding mass transport rate, it is assumed to be controlled by oxygen diffusion in the GDL.

The Damköhler number Da for the cell has been represented in Fig. 6 (bottom), where Da numbers obtained are ranging from 25 to 100, showing a clear dominance of the diffusion process in terms of time constants. The exception is the operation with pure oxygen, where the absence of a diffusion-limiting process for the oxygen transport leads to null Damkhöler numbers for low and medium current densities, where the oxygen mass flux demanded by the electrochemical reaction is still not as high as to cause mass transfer limitations under pure oxygen conditions. The Damkhöler number is generally diminishing with current density, which is mainly the result of the smaller diffusion time constants. The conditions leading to the highest Da values are depending on the range of the current density being considered. Dry conditions (higher temperature or lower reactants RH) are causing higher Da values at low current densities of 0.2 A/cm^2. However, conditions leading to the smallest values of Da at such current densities (corresponding to pure oxygen and higher reactants RH) are resulting in the highest Da values at high current densities of 1.5 A/cm^2 (among the IV curves with available data at such current density).

5. Conclusions

The performance of a 50 cm^2 PEM fuel cell with serpentine flow field under different operating conditions was analysed via experimental measurements. Electrochemical Impedance Spectroscopy (EIS) was also used in order to gain a better insight into the different polarization contributions and trends. The polarization curves were determined, as well as Nyquist plots and High Frequency Resistance (HFR) values.

Performance trends with respect to variations in the operating conditions (cell temperature and backpressure, reactants RH, cathode stoichiometry, air/oxygen operation) were analysed and discussed, in light of the results obtained for IV curves, HFR values, and Nyquist plots. Higher HFR values were obtained for curves with lower reactants RH (30%) and higher cell temperatures (75 °C). The cell performance with pure oxygen was obviously the highest, followed by the operation with air at higher pressures (1.0 bar vs. 0.5 bar). EIS results did not produced any observable low frequency arc associated to mass transport polarization when pure oxygen was used, even at high current densities (100 A or 2.0 A/cm^2). The effect of RH on the cathode polarization and on the ohmic resistance was clearly observed in the Nyquist plots and polarization curves.

The time constants associated to the electrochemical and diffusion processes within the cell were determined by using the Distribution of Relaxation Times, where the impedance spectra were used as input. The comprehensive operating conditions used allowed for an understanding on how the different relevant operating variables are influencing the time constants. Pressure, temperature, relative humidity, cathode stoichiometry, oxygen concentration and current density were analysed. The information obtained is fundamental for quantitatively describing the individual losses and to clearly determine the factors limiting performance, so that a more detailed knowledge can be achieved for progressing towards a better fine-tuning of the properties of the cell components that better perform for a given set of operating conditions (and vice-versa, the optimum operating conditions that better perform for a given cell design). This work has presented for the first time the application of the DRT method for determining time constants of diffusion and electrochemical processes in PEM Fuel Cells 50 cm^2, which is a representative size between lab-scale and industry-scale fuel cells.

Credit author statement

Alfredo Iranzo: Conceptualization; Data curation; Formal analysis; Funding acquisition; Investigation; Methodology; Project administration; Supervision; Writing – original draft; Writing – review & editing. Sergio Jesús Navas: Data curation; Formal analysis; Investigation; Software; Visualization; Writing – original draft. Felipe Rosa: Funding acquisition; Project administration; Resources; Supervision. Mohamed R. Berber: Funding acquisition; Investigation; Project administration; Resources; Writing – review & editing.

Declaration of competing interest

The authors declare that they have no known competing financial interests or personal relationships that could have appeared to influence the work reported in this paper.

Acknowledgements

This work has been developed thanks to the funding of the Spanish Ministry of Science, Innovation and Universities (grant ENE2017-91159-EXP and PID2019-104441RB-I00), the Spanish Ministry of Economy and Competitiveness (grant UNSE15-CE2962), all projects funded by AEI/FEDER UE, and the Consejería de Economía, Conocimiento, Empresas y Universidad, PAIDI 2020 program by Junta de Andalucía (PY20 RE026 AICIA), co-funded with ERDF funds. The authors extend their appreciation to the Deputyship for Research & Innovation, Ministry of Education in Saudi Arabia for co-funding this research work through the project number “375213500". The authors also would like to extend their sincere appreciation to the central laboratory at Jouf University for the support of this study.

Appendix C. Supplementary data

Supplementary data to this article can be found online at https://doi.org/10.1016/j.energy.2021.119833.

Appendix A

The main elements of the test bench and are presented in Fig. A1, where the reactant gases supply, Mass Flow Controllers, humidifiers (bubblers) and backpressure regulators are observed in the Balance of Plant. Fig. A2 depicts the disposition of the fuel cell set-up, together with the main electrical components: Programmable Power Supply MAGNA POWER SL5-250/UI, Electronic Load ADAPTATIVE POWER 5L18-24, and Frequency Response Analyzer NEWTONS4TH PSM1700. The graphite Bipolar Plates used for the 50 cm^2 fuel cell are presented in Fig. A3, featuring the characteristics of the serpentine flow field.

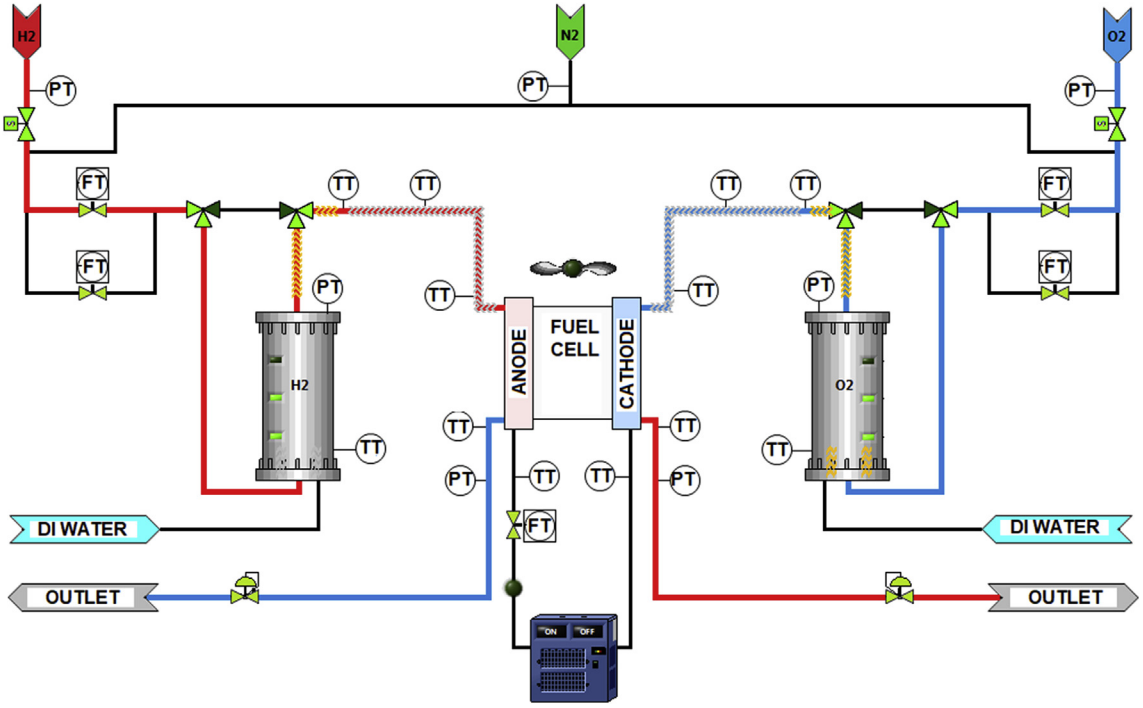

Fig. A.1. P&I Diagram of the fuel cell test bench used in the experimental section (image reproduced from Ref. [82]).

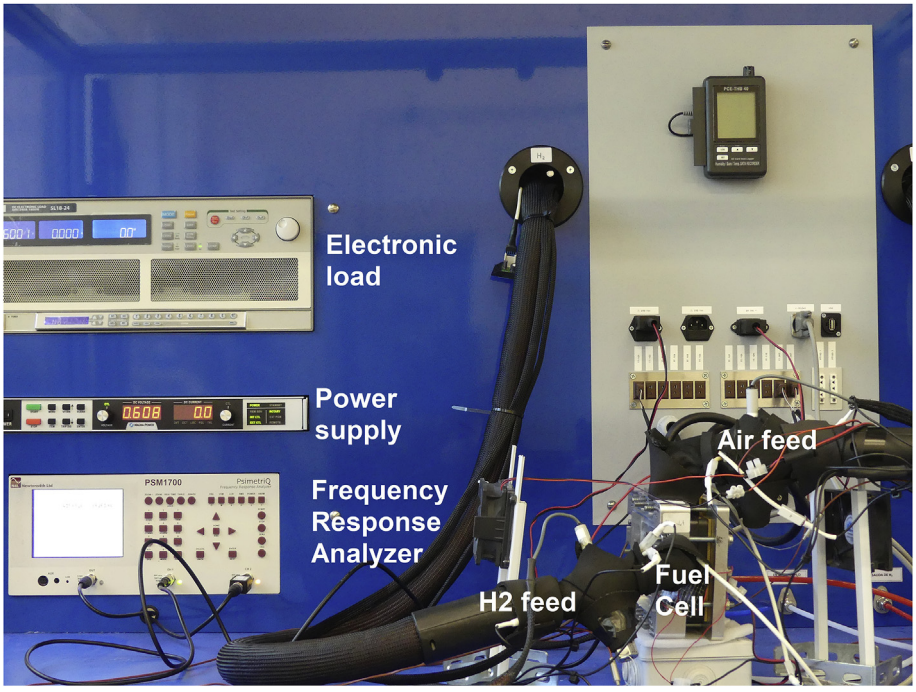

Fig. A.2. Fuel Cell set-up in the test bench (image reproduced from Ref. [83]).

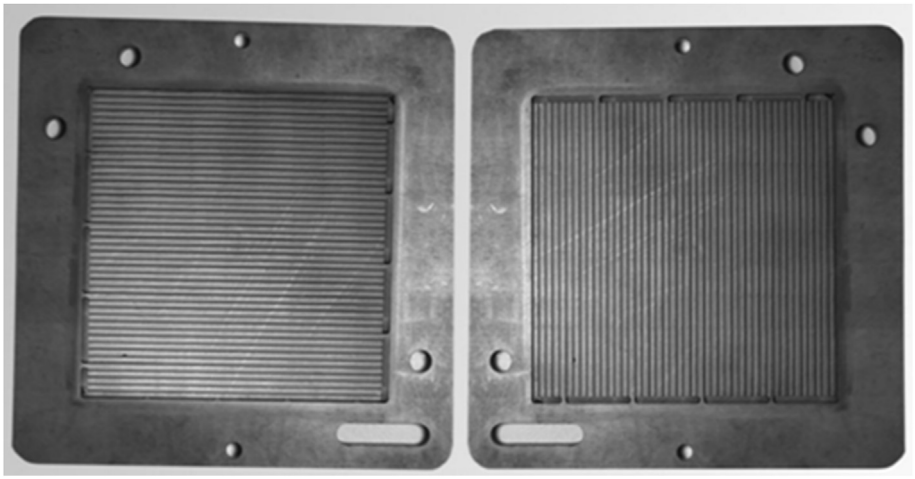

Fig. A.3. Fuel Cell Bipolar Plates with serpentine flow field used in the experiments, from ElectroChem Inc. (image reproduced from Ref. [83]). Anode flow field is featuring horizontal channels. Cathode flow field is featuring vertical channels.

Appendix B

The pressure drop measured at the cathode side of the cell is depicted in Fig. B1 for the experiments reported in Fig. 1.

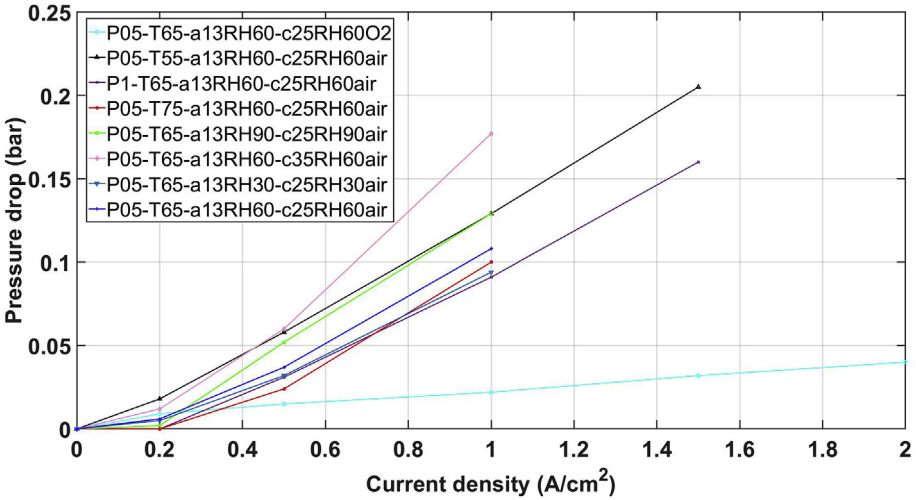

Fig. B.1. Pressure drop measured at the cathode side of the cell during the recording of the polarization curves.

References

[1] Sharaf Omar Z, Orhan Mehmet F. An overview of fuel cell technology: fundamentals and applications. Renew Sustain Energy Rev 2014;32:810–53.

[2] Ou K, Yuan W-W, Kim Y-B. Development of optimal energy management for a residential fuel cell hybrid power system with heat recovery. Energy 2021;219:119499.

[3] Calise F, Ferruzzi G, Vanoli L. Transient simulation of polygeneration systems based on PEM fuel cells and solar heating and cooling technologies. Energy 2012;41:18–30.

[4] Al-Nimr MA, Bukhari M, Mansour M. M. A combined CPV/T and ORC solar power generation system integrated with geothermal cooling and electrolyser/fuel cell storage unit. Energy 2017;133:513–24.

[5] Guo X, Zhang H, Yuan J, Wang J, Zhao J, Wang F, et al. Performance assessment of a combined system consisting of a high-temperature polymer electrolyte membrane fuel cell and a thermoelectric generator. Energy 2019;179:762–70.

[6] Thompson Simon T, James Brian D, Huya-Kouadio Jennie M, Houchins Cassidy, Papageorgopoulos Dimitrios. Direct hydrogen fuel cell electric vehicle cost analysis: system and high-volume manufacturing description, validation, and outlook. J Power Sources 2018;399:304–13.

[7] Leo TJ, Durango JA, Navarro E. Exergy analysis of PEM fuel cells for marine applications. Energy 2010;35:1164–71.

[8] Hsieh C-Y, Pei P, Bai Q, Su A, Weng F-B, Lee C-Y. Results of a 200 hours lifetime test of a 7 kW Hybrid–Power fuel cell system on electric forklifts. Energy 2021;214:118941.

[9] Alaswad A, Baroutaji A, Achour H, Carton J, Olabi AG. Developments in fuel cell technologies in the transport sector. Int J Hydrogen Energy 2016;41:16499–508.

[10] Ahluwalia Rajesh K, Wang Xiaohua. Fuel cell systems for transportation: status and trends. J Power Sources 2008;177:167–76.

[11] Olabi AG, Wilberforce T, Abdelkareem MA. Fuel cell application in the automotive industry and future perspective. Energy 2020;214:118955.

[12] Haslam Gareth E, Jupesta Joni, Govindan Parayil. Assessing fuel cell vehicle innovation and the role of policy in Japan, Korea, and China. Int J Hydrogen Energy 2012;37:14612–23.

[13] Xu Xinhai, Xu Ben, Dong Jun, Liu Xiaotong. Near-term analysis of a roll-out strategy to introduce fuel cell vehicles and hydrogen stations in Shenzhen China. Appl Energy 2017;196:229–37.

[14] Liu Feiqi, Zhao Fuquan, Liu Zongwei, Han Hao. The impact of fuel cell vehicle deployment on road transport greenhouse gas emissions: the China case. Int J Hydrogen Energy 2018;43:22604–21.

[15] Scott Hardman, Gil Tal. Who are the early adopters of fuel cell vehicles? Int J

Hydrogen Energy 2018;43:17857–66.
[16] Itaoka Kenshi, Saito Aya, Sasaki Kazunari. Public perception on hydrogen infrastructure in Japan: influence of rollout of commercial fuel cell vehicles. Int J Hydrogen Energy 2017;42:7290–6.
[17] Chang Xiaoying, Ma Tao, Wu Ran. Impact of urban development on residents' public transportation travel energy consumption in China: an analysis of hydrogen fuel cell vehicles alternatives. Int J Hydrogen Energy 2019;44:16015–27.
[18] Kang Min Jung, Park Heejun. Impact of experience on government policy toward acceptance of hydrogen fuel cell vehicles in Korea. Energy Pol 2011;39:3465–75.
[19] Zamel Nada, Li Xianguo. Life cycle comparison of fuel cell vehicles and internal combustion engine vehicles for Canada and the United States. J Power Sources 2006;162:1241–53.
[20] Nazir H, Muthuswamy N, Louis C, Jose S, Prakash J, Buan MEM, et al. Is the H2 economy realizable in the foreseeable future? Part I: H2 production methods. Int J Hydrogen Energy 2020;45:13777–88.
[21] Nazir H, Muthuswamy N, Louis C, Jose S, Prakash J, Buan MEM, et al. Is the H2 economy realizable in the foreseeable future? Part II: H2 storage, transportation, and distribution. Int J Hydrogen Energy 2020;45:20693–708.
[22] Nazir H, Muthuswamy N, Louis C, Jose S, Prakash J, Buan MEM, et al. Is the H2 economy realizable in the foreseeable future? Part III: H2 usage technologies, applications, and challenges and opportunities. Int J Hydrogen Energy 2020;45:28217–39.
[23] Berber MR, Fujigaya T, Nakashima N. A potential polymer formulation of a durable carbon-black catalyst with a significant fuel cell performance over a wide operating temperature range. Mater Today Energy 2018;10:161–8.
[24] Berber MR, Mustafa MY. Poly[2,2′-(4,4′-bipyridine)-5,5′-bibenzimidazole] functionalization of carbon black for improving the oxidation stability and oxygen reduction reaction of fuel cells. RSC Adv 2020;10:30776–84.
[25] Wu Jinfeng, Xiao Zi Yuan, Wang Haijiang, Blanco Mauricio, Zhang Jiujun. Diagnostic tools in PEM fuel cell research: Part I Electrochemical techniques. Int J Hydrogen Energy 2008;33:1735–46.
[26] Neyerlin KC, Gu W, Jorne J, Gasteiger HA. Determination of catalyst unique parameters for the oxygen reduction reaction in a PEMFC. JElectrochemSoc 2006;153:A1955–63.
[27] Iranzo Alfredo, Muñoz Miguel, López Eduardo, Pino Javier, Rosa Felipe. Experimental fuel cell performance analysis under different operating conditions and bipolar plate designs. Int J Hydrogen Energy 2010;35:11437–47.
[28] Fouquet N, Doulet C, Nouillant C, Dauphin-Tanguy G, Ould-Bouamama B. Model based PEM fuel cell state-of-health monitoring via ac impedance measurements. JPower Sources 2006;159:905–13.
[29] Wasterlain S, Candusso D, Harel F, François X, Hissel D. Diagnosis of a fuel cell stack using electrochemical impedance spectroscopy and Bayesian networks. In: IEEE vehicle power and propulsion conference; 2010. p. 1–6. Lille.
[30] Jeppesen C, Araya SS, Sahlin sL, Thomas S, Andreasen SJ, Kær SK. Fault detection and isolation of high temperature proton exchange membrane fuel cell stack under the influence of degradation. J Power Sources 2017;359:37–47.
[31] Iranzo Alfredo, Muñoz Miguel, Javier Pino Fco, Rosa Felipe. Non-dimensional analysis of PEM fuel cell phenomena by means of AC impedance measurements. J Power Sources 2011;196:4264–9.
[32] Ivers-Tiffée E, Weber A, Schichlein H. Electrochemical impedance spectroscopy. In: Vielstisch W, Yokokawa H, Gasteiger HA, editors. Handbook of fuel cells. Chichester, UK: John Wiley; 2003. p. 220–35.
[33] Yuan X, Wang H, Colin Sun J, Zhang J. AC impedance technique in PEM fuel cell diagnosis-A review. Int J Hydrogen Energy 2007;32:4365–80.
[34] Seyed Mohammad Rezaei Niya, Hoorfar Mina. Study of proton exchange membrane fuel cells using electrochemical impedance spectroscopy technique – a review. J Power Sources 2013;240:281–93.
[35] Asghari Saeed, Ali Mokmeli, Samavati Mahrokh. Study of PEM fuel cell performance by electrochemical impedance spectroscopy. Int J Hydrogen Energy 2010;35:9283–90.
[36] Liu F, Yi B, Xing D, Yu J, Hou Z, Fu Y. Development of novel self-humidifying composite membranes for fuel cells. J Power Sources 2003;124:81–90.
[37] Markiewicz M, Zalitis C, Kucernak A. Performance measurements and modelling of the ORR on fuel cell electrocatalysts – the modified double trap model. Electrochim Acta 2015;179:126–36.
[38] Leonide A, Sonn V, Weber A, Ivers-Tiffée E. Evaluation and modeling of the cell resistance in anode-supported solid oxide fuel cells. J Electrochem Soc 2008;155:B36–41.
[39] Illig J, Ender M, Chrobak T, Schmidt JP, Klotz D, Ivers-Tiffee E. Separation of charge transfer and contact resistance in LiFePO4-cathodes by impedance modelling. J Electrochem Soc 2012;159:A952–60.
[40] Weiß Alexandra, Schindler Stefan, Galbiati Samuele, Danzer Michael A, Zeis Roswitha. Distribution of relaxation times analysis of high-temperature PEM fuel cell impedance spectra. Electrochim Acta 2017:391–8. 23010.
[41] Heinzmann Marcel, Weber André, Ivers-Tiffée Ellen. Advanced impedance study of polymer electrolyte membrane single cells by means of distribution of relaxation times. J Power Sources 2018;402(31):24–33.
[42] Heinzmann Marcel, Weber André, Ivers-Tiffée Ellen. Impedance modelling of porous electrode structures in polymer electrolyte membrane fuel cells. J Power Sources 2019;444(31):227279.
[43] Wan TH, Saccoccio M, Chen C, Ciucci F. Influence of the discretization methods on the distribution of relaxation times deconvolution: implementing radial Basis functions with DRT tools. Electrochim Acta 2015;184:483–99.
[44] Feb. https://ciucci.org/project/drt/; 2020.
[45] Saccoccio M, Wan TH, Chen C, Ciucci F. Optimal regularization in distribution of relaxation times applied to electrochemical impedance spectroscopy: ridge and lasso regression methods – a theoretical and experimental study. Electrochim Acta 2014;147:470–82.
[46] Ciucci F, Chen C. Analysis of electrochemical impedance spectroscopy data using the distribution of relaxation times: a bayesian and hierarchical bayesian approach. Electrochim Acta 2015;167:439–54.
[47] Tang Z, Huang QA, Wang YJ, Zhang F, Li W, Li A, Zhang L, Zhang J. Recent progress in the use of electrochemical impedance spectroscopy for the measurement, monitoring, diagnosis and optimization of proton exchange membrane fuel cell performance. J Power Sources 2020;468:228361.
[48] Xing L, Shi W, Das PK, Scott K. Inhomogeneous distribution of platinum and ionomer in the porous cathode to maximize the performance of a PEM fuel cell. AIChE J 2017;63(11):4895–910.
[49] Xuan J, Wang H, Leung DYC, Leung Michael KH, Xu Hong, Zhang L, Shen Y. Theoretical Graetz-Damköhler modeling of an air-breathing microfluidic fuel cell. J Power Sources 2013;231:1–5.
[50] Wang Y, Chen KS. Elucidating two-phase transport in a polymer electrolyte fuel cell, Part 1: characterizing flow regimes with a dimensionless group. Chem Eng Sci 2011;66:3557–67.
[51] Gyenge EL. Dimensionless numbers and correlating equations for the analysis of the membrane-gas diffusion electrode assembly in polymer electrolyte fuel cells. J Power Sources 2005;152(1–2):105–21.
[52] The fuel cell testing and standarization network. EU FP5 Project ENG2-CT-2002-20657., FCTESTNET Test procedures draft v1, vol. 4; 2006.
[53] FCTESTQA Test protocol. Testing the voltage and power as function of current density. Polarisation curve for a PEFC single cell. Test Module PEFC SC 5-2. European Commission, Joint Research Centre, Institute for Energy; 2010.
[54] Mench M. Fuel cell engines. first ed. Wiley; 2008.
[55] Barbir F. PEM fuel cells: theory and practice. first ed. Elsevier Academic; 2005.
[56] Asghari Saeed, Ali Mokmeli, Samavati Mahrokh. Study of PEM fuel cell performance by electrochemical impedance spectroscopy. Int J Hydrogen Energy 2010;35:9283–90.
[57] Chang Hao-Ming, Lin Chien-Wei, Chang Min-Hsing, , Huan-Ruei Shiu, Chang Wen-Chen, Tsau Fang-Hei. Optimization of polytetrafluoroethylene content in cathode gas diffusion layer by the evaluation of compression effect on the performance of a proton exchange membrane fuel cell. J Power Sources 2011;196:3773–80.
[58] Danzer Michael A, Hofer Eberhard P. Analysis of the electrochemical behaviour of polymer electrolyte fuel cells using simple impedance models. J Power Sources 2009;190:25–33.
[59] Yan Xiqiang, Hou Ming, Sun Liyan, Dong Liang, Shen Qiang, Xu Hongfei, Ming Pingwen, Yi Baolian. AC impedance characteristics of a 2 kW PEM fuel cell stack under different operating conditions and load changes. Int J Hydrogen Energy 2007;32:4358–64.
[60] Yin K-M, Chang C-P. Effects of humidification on the membrane electrode assembly of proton exchange membrane fuel cells at relatively high cell temperatures. Fuel Cell 2011;11:888–96.
[61] Schneider IA, Bayer MH, Wokaun A, Scherer GG. Impedance response of the proton exchange membrane in polymer electrolyte fuel cells. J Electrochem Soc 2008;155:B783–92.
[62] Kadyk Thomas, Hanke-Rauschenbach Richard, Sundmacher Kai. Nonlinear frequency response analysis of PEM fuel cells for diagnosis of dehydration, flooding and CO-poisoning. J Electroanal Chem 2009;630:19–27.
[63] Rezaei Niya SM, Phillips RK, Hoorfar M. Process modeling of the impedance characteristics of proton exchange membrane fuel cells. Electrochim Acta 2016;191:594–605.
[64] Dai Wei, Wang Haijiang, Yuan Xiao-Zi, Martin Jonathan J, Ma Jianxin. A review on water balance in the membrane electrode assembly of proton exchange membrane fuel cells. Int J Hydrogen Energy 2009;34:9461–78.
[65] Iranzo A, Salva JA. Effect of anode/cathode operating pressures on the liquid water content and performance of a PEM fuel cell. Fuel Cell 2018;18:742–7.
[66] Springer TE, Zowodzinski TA, Gottesfeld S. Polymer electrolyte fuel cell model. J Electrochem Soc 1991;138:2334–42.
[67] Li H, Tang Y, Wang Z, Shi Z, Wu S, Song D, et al. A review of water flooding issues in the proton exchange membrane fuel cell. J Power Sources 2008;178:103–17.
[68] Springer TE, Zawodzinski TA, Wilson MS, Gottesfeld S. Characterization of polymer electrolyte fuel cells using AC impedance spectroscopy. J Electrochem Soc 1996;143:587–99.
[69] Cooper KR, Smith M. Electrical test methods for on-line fuel cell ohmic resistance measurement. J Power Sources 2006;160:1088–95.
[70] Liu Y, Murphy MW, Baker DR, Gu W, Jib C, Jorne J, Gasteiger HA. Proton conduction and oxygen reduction kinetics in PEM fuel cell cathodes: effects of ionomer-to-carbon ratio and relative humidity. J Electrochem Soc 2009;156:B970–80.
[71] Neyerlin KC, Gasteiger HA, Mittelsteadt CK, Jorne J, Gu W. Effect of relative humidity on oxygen reduction kinetics in a PEMFC. J Electrochem Soc 2005;152:A1073–80.
[72] Xu H, Song Y, Kunz HR, Fenton JM. Effect of elevated temperature and reduced relative humidity on ORR kinetics for PEM fuel cells. J Electrochem Soc 2005;152:A1828–36.
[73] Zamel N, Li X. Effective transport properties for polymer electrolyte

membrane fuel cells - with a focus on the gas diffusion layer. Prog Energy Combust Sci 2013;39:111–46.
[74] Jiao K, Li X. Water transport in polymer electrolyte membrane fuel cells. Prog Energy Combust Sci 2011;37:221–91.
[75] Iranzo A, Boillat P, Oberholzer P, Guerra J. A novel approach coupling neutron imaging and numerical modelling for the analysis of the impact of water on fuel cell performance. Energy 2014;68:971–81.
[76] Iranzo A, Boillat P. CFD simulation of the transient gas transport in a PEM fuel cell cathode during AC impedance testing considering liquid water effects. Energy 2018;158:449–57.
[77] Nam JH, Kaviany M. Effective diffusivity and water-saturation distribution in single- and two-layer PEMFC diffusion medium. Int J Heat Mass Tran 2003;46:4595–611.
[78] Um S, Wang C-Y, Chen KS. Computational fluid dynamics modeling of proton exchange membrane fuel cells. J Electrochem Soc 2000;147(12):4485–93.
[79] Wang C-Y. Fundamental models for fuel cell engineering. Chem Rev 2004;104:4727–65.
[80] Iranzo A, Boillat P, Rosa F. Validation of a three dimensional PEM fuel cell CFD model using local liquid water distributions measured with neutron imaging. Int J Hydrogen Energy 2014;39:7089–99.
[81] Gasteiger HA, Kocha SS, Sompalli B, Wagner FT. Activity benchmarks and requirements for Pt, Pt-alloy, and non-Pt oxygen reduction catalysts for PEMFCs. Appl Catal B Environ 2005;56:9–35.
[82] Ramírez-Cruzado A, Ramírez-Peña B, Vélez-García R, Iranzo A, Guerra J. Data from experimental analysis of the performance and load cycling of a polymer electrolyte membrane fuel cell. Data 2020;5(2):47.
[83] Ramírez-Cruzado A, Ramírez-Peña B, Vélez-García R, Iranzo A, Guerra J. Experimental analysis of the performance and load cycling of a polymer electrolyte membrane. Fuel Cell, Processes 2020;8(5):608.